Machine Learning Small Polaron Dynamics

Viktor C. Birschitzky,[1] Luca Leoni,[2] Michele Reticcioli,[1] and Cesare Franchini[1,2,*]
[1]University of Vienna, Faculty of Physics and Center for Computational Materials Science, Vienna, Austria
[2]Department of Physics and Astronomy "Augusto Righi," Alma Mater Studiorum—Università di Bologna, Bologna, 40127 Italy

(Received 11 September 2024; revised 16 April 2025; accepted 28 April 2025; published 27 May 2025)

Polarons are crucial for charge transport in semiconductors, significantly impacting material properties and device performance. The dynamics of small polarons can be investigated using first-principles molecular dynamics. However, the limited timescale of these simulations presents a challenge for adequately sampling infrequent polaron hopping events. Here, we introduce a message-passing neural network combined with first-principles molecular dynamics within the Born-Oppenheimer approximation that learns the polaronic potential energy surface by encoding the polaronic state, allowing for simulations of polaron hopping dynamics at the nanosecond scale. By leveraging the statistical significance of the long timescale, our framework can accurately estimate polaron (anisotropic) mobilities and activation barriers in prototypical polaronic oxides across different scenarios (hole polarons in rocksalt MgO and electron polarons in pristine and F-doped rutile TiO_2) within experimentally measured ranges.

DOI: 10.1103/PhysRevLett.134.216301

Introduction—A small polaron is a spatially localized quasiparticle that forms in polarizable materials due to the attraction of an excess charge carrier to its own self-induced lattice distortion [1–5]. When thermally activated, small polarons can travel through the crystal, constituting one of the primary charge transport mechanisms. In addition, they play a crucial role in various physical and technologically significant processes, such as optical excitations [6–8], (photo)catalysis [9–12], photovoltaic applications [13], and device functioning [14]. Several theories have been developed to understand and predict small polaron mobility [5], including Marcus-Emin-Holstein-Austin-Mott (MEHAM) theory [15–19], density functional theory (DFT) [20,21], diagrammatic Monte Carlo [22], and dynamical mean field theory [23]. Moreover, alternative approaches have been proposed to study large or intermediate polaron mobility [5,24–30].

Small polaron transfer can occur either via hopping mechanism or through delocalization in the conduction band [31–33]. As depicted in Fig. 1, thermally activated small polaron hopping is either adiabatic or diabatic, depending on the strength of the electronic coupling between the initial and final states. In the adiabatic regime, the polaron charge transfers smoothly to a neighboring site, while in the diabatic regime, the charge is transferred instantaneously [16,19]. Unlike conduction band diffusion, for which mobility is difficult to estimate [34], polaron hopping mobility can be obtained using MEHAM theory and the Einstein relation [35], typically by calculating the activation energy through quasistatic linear interpolation between initial and final states along specific polaron transport paths [20]. While MEHAM theory allows for a rigorous treatment of the electronic coupling of initial and final states and quantitatively describes both adiabatic and diabatic polaron transfer, the approach limits the comprehensive exploration of diffusion pathways and introduces approximations for the preexponential factor [33].

The dynamical aspects of polarons can be explored using first-principles molecular dynamics (FPMD), which is typically based on DFT within the Born-Oppenheimer (BO) approximation. FPMD has proven highly successful in assessing dynamical properties of materials [36] and

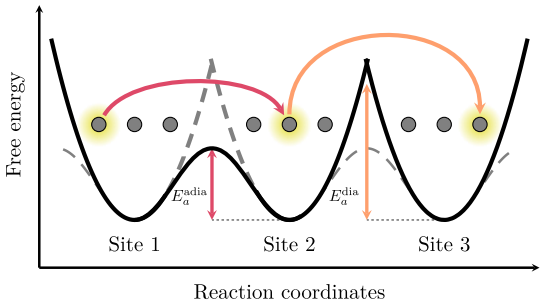

FIG. 1. Schematic description of adiabatic and nonadiabatic hopping transitions from one site to its neighbor, with activation energy E_a^{adia} and E_a^{dia}. Small filled circles symbolize lattice sites, whereas the light clouds represent the polaron charge.

*Contact author: cesare.franchini@univie.ac.at

has been extensively used to study small polarons, offering insights into their activation energies, hopping dynamics, configurational space, and charge recombination [21,37–44]. While a rigorous treatment of diabatic electron transfer (i.e., tunneling) requires methods beyond the BO approximation [20,45–47], FPMD remains a powerful tool for accurately describing adiabatic electron transfer. FPMD can qualitatively capture diabatic transfer (hopping from one polaronic potential energy surface to another) when the transfer occurs rapidly enough [48]. However, despite its renowned computational efficiency, FPMD is limited by the accessible timescale, typically spanning only a few picoseconds.

Since the pioneering works on neural network potentials [49] and Gaussian approximation potentials [50], machine learning (ML) has transformed FPMD [51,52]. Contemporary ML-based potential energy surface models often employ message-passing neural networks and incorporate equivariance into their architecture [53,54], enhancing both accuracy and data efficiency in learning the potential energy surface. These models enable the assessment of material properties at a fraction of the cost of direct DFT evaluation, extending simulation times or system sizes while preserving DFT accuracy.

Enhancing the capability of ML-based MD (MLMD) to account for polaron dynamics is complex and remains an open challenge. While effects such as the prediction of local magnetic moments [55] and nonlocal charge transfer [56] have been incorporated into ML-based force fields using local environment descriptors, these methods do not explicitly enforce charge conservation, rendering them unsuitable for simulating small polaron dynamics. To address charge conservation, global charge equilibration schemes have been proposed that allocate charge based on the electronegativity at each site [57,58]. However, these approaches may lead to unphysical charge transport mechanisms due to their global nature and the potential for spurious responses to thermal fluctuations in local environments.

In this Letter, we present the ML package LEOPOLD (LEarning Of POLaron Dynamics), designed to accurately model small polaron dynamics. The architecture, implemented in JAX [59], is built on a modified version of the Neural Equivariant Interatomic Potential (NEQUIP) architecture [54] trained on Vienna *Ab initio* Simulation Package (VASP) data [60,61]. We introduce two key features to account for polaron transport: (i) explicit charge state encoding [62] to ensure charge conservation and identify polaronic sites, and (ii) direct prediction of site occupation to track polaron hopping and regularize the descriptor [56]. The architecture is described in detail in the End Matter. The model is assessed by considering three different systems: hole polaron in rocksalt MgO ($MgO + h^+$ in oxygen p orbitals), electron polaron in rutile TiO_2 ($TiO_2 + e^-$ in titanium d orbitals), and combined electron polaron-defect dynamics in F-doped TiO_2 ($TiO_{1.99}F_{0.01}$). To describe the coupled dopant-polaron system, we employ an active learning scheme that effectively addresses the configurational sampling problem and accurately reproduces the correct polaron distribution in a defective system [see Supplemental Material (SM) for details on the employed methodology [63]]. Our approach can predict polaron hopping events, thereby enhancing the sampling of hopping trajectories and enabling nanosecond-scale simulations to extract polaronic mobility, activation energies (E_a), and transition pathways.

Results—Figure 2(a) displays a hopping event—as generated by LEOPOLD in an MLMD simulation and reproduced in DFT—based on the dynamical magnetization and demagnetization of two neighboring sites in $MgO + h^+$ (other site's magnetizations are close to 0 and omitted for clarity). Initially ($t = 0$), the polaron charge is localized on one site and becomes progressively destabilized due to thermal motion. At the crossing point, the polaron is shared between two sites until it fully localizes on the final site ($t \approx 40$ fs). To accurately reproduce these hopping processes by our ML model, we initially train LEOPOLD on one FPMD run unavoidably including only a few hopping events and concurrently use the trained model to simulate polaron dynamics in an ML-based MD run. As hopping is a relatively rare event in the ps timescale, the initial dataset may not capture all possible transition pathways. To address this, we employ an active learning scheme by extracting hopping processes from the ML-based run and calculating them at the reference DFT + U level. This extended dataset is then used to retrain the model iteratively. While this approach is not necessarily comprehensive, we found that after a few active learning loops, hopping events were well sampled and the model did not produce new symmetrically inequivalent transition pathways.

The results are presented in Fig. 2(b), showing the local magnetization of sites involved in hopping events as produced by LEOPOLD and confirmed by DFT for $MgO + h^+$. Achieved errors are within the expected ranges [55,56] as detailed in SM [63]. From approximately 50 hopping events extracted at temperatures ranging from 100 to 600 K from 10 ns MLMD runs, we identified two key characteristics of the hopping behavior in $MgO + h^+$: (i) in the rocksalt octahedral symmetry, the oxygen p states hosting the hole polaron are threefold degenerate, which allows for only one symmetrically inequivalent nearest-neighbor hopping pathway along the [110] direction; (ii) the polaronic transition between sites occurs adiabatically [16] following a hopping mechanism similar to the one shown in Fig. 2(a).

In contrast, rutile TiO_2 exhibits more complex structural symmetries and hopping processes. Figures 2(c) and 2(d) summarize the results, where we focus our discussion to the [001], [110], and [111] hopping paths within a single $(1\bar{1}0)$

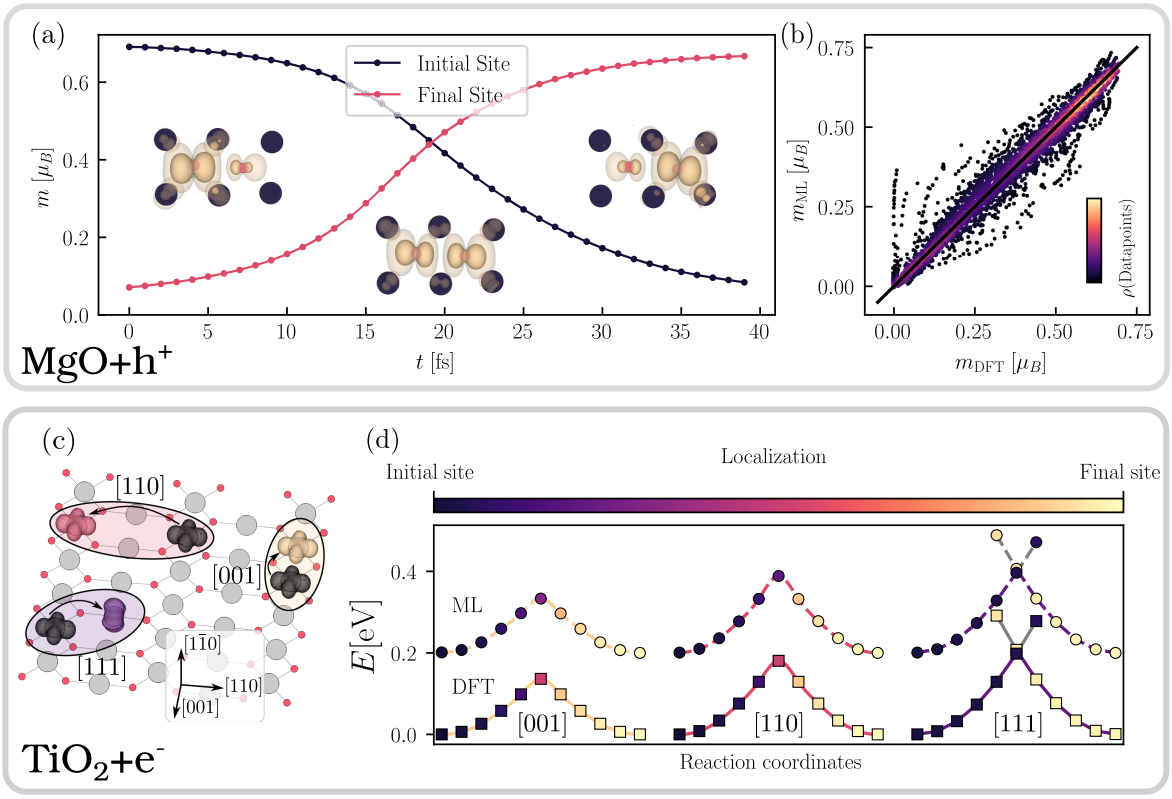

FIG. 2. Polaron hopping from ML and DFT for hole polarons in MgO and electron polarons in TiO_2. (a) Hopping event extracted from MLMD through the evolution of the local site-projected magnetization m. Polaron charge isosurfaces are shown for the initial, intermediate (crossing point), and final states. (b) Comparison of m_{DFT} and m_{ML} of 50 hopping events extracted from MLMD at various temperatures. m is only displayed for the involved sites ($m > 0.3$ at any time step in the hopping event) and the data point density is encoded via the color scale. (c) Possible polaron transitions to neighboring sites along three different directions ([001], [110], [111]) in TiO_2 shown for a single TiO_2 $(1\bar{1}0)$ layer. (d) Comparison between DFT (full lines, square marker) and ML (dashed lines, round marker) activation energies for the three different transition directions as approximated by linear interpolation. The color code indicates the site-projected charge localization defined through the magnetization m as $(m_{final} - m_{initial} + 1)/2$ (0, full localization on the initial site; 1, full localization on the final site). At DFT-level [001] and [110] pathways show adiabatically coupled transition states (polaron shared between initial and final sites), while [111] transition is characterized by an instantaneous hopping at the crossing point.

plane for simplicity. The electron polaron occupies a single t_{2g} orbital, where the triple degeneracy is lifted by an axial elongation of the octahedron [78,79]. This orbital symmetry favors polaron migration along the [001] and [110] pathways. Polaron transport along [111] requires a 90° rotation of the polaron orientation, making these transport directions less probable [20]. These considerations are well reflected in our MLMD data at high temperatures, showing 74.3% of transitions along the [001] direction, 25.5% along the [110] direction, and 0.2% along the [111] direction.

Interestingly, unlike MgO, hops along both adiabatic and diabatic transition pathways (as previously determined by MEHAM theory [20]) are observed. To better describe these different processes, we performed quasistatic calculations, i.e., we calculated energy and polaron localization on structures obtained by linear interpolation of atomic coordinates between initial and final states. As shown in Fig. 2(d) the ML results are in excellent agreement with DFT calculations. Transport along the dominant [001] direction is adiabatic, as deduced by the continuous change of the site-projected magnetization during the hopping process for intermediate interpolated structures between nearest-neighbor Ti sites [see gradient bar in Fig. 2(d) or SM [63]]. Transitions along the less favorable [110] direction between third nearest-neighbor Ti sites can still be classified as adiabatic, as indicated by the smooth charge transfer, as depicted by the color coding in Fig. 2(d). However, the electronic coupling between the initial and final states, which are 6.4 Å apart, is low, as suggested by the more pronounced peak in the corresponding energy curve. The less frequent migration pathway along the [111] direction, which requires a modification of the polaron orbital symmetry, is characterized by a diabatic process [20] associated with a sudden change in the magnetic moment and instantaneous hop from the initial and final states.

Remarkably, even though electron delocalization associated with migrations along the [110] and [111] directions is not fully captured by our integer charge state assumption,

LEOPOLD is still able to qualitatively reproduce the relative frequency of adiabatic and diabatic events [20]. In particular, while the hopping events that exhibit some degree of charge delocalization may cause nonphysical oscillations in our ML model, they remain meaningful as long as the final localization site is consistent with DFT predictions and the transition features a well-sampled energetic barrier. Furthermore, the small timescale of unphysical oscillations, compared to the large timescales considered, renders the impact on physical observables computed on the obtained polaron trajectory insignificant (see SM for further discussion [63]).

The polaron transport data generated by LEOPOLD enable an accurate evaluation of diffusion properties. By using statistical quantities such as the mean squared displacement (see SM for details [63]), we can evaluate polaron mobility and activation energies, refining the results obtained by quasi-statical models. Figure 3 collects the mobility computed from canonical ensemble (i.e., constant number of particles N, volume V and temperature T) simulations at various temperatures in MgO, TiO_2, and $TiO_{1.99}F_{0.01}$ for up to 10 ns. Mobility increases with temperature, as expected for small polaron transport [5]. The predicted μ and E_a for rutile TiO_2 fall within the experimentally reported range of 0.01–10.0 cm^2/Vs [64,80–83] and agree with previous MEHAM theory work [20]. The reduced mobility in $TiO_{1.99}F_{0.01}$ is attributed to the attractive interaction between electron polarons and positively charged defects, which typically decreases polaron diffusion. Activation energies in $TiO_2 + e^-$ align with theoretical values from nudged elastic band calculations ($E_a = 58$ meV using hybrid functional) [80]. We note that our model takes into account several types of hopping processes, with different energy barriers, while quasistatic approaches typically consider only one or few processes. Near room temperature conductivity measurements for MgO reported difficulties in obtaining reproducible results [65–67], but activation energies from MLMD simulations agree well with theoretical values based on nudged elastic band for $MgO + h^+$ [65] ($E_a = 110$ meV).

We now consider in greater detail a more realistic scenario in which the excess charge forming the polaron is introduced via chemical doping, specifically by substituting an oxygen atom with a fluorine atom in rutile TiO_2 ($TiO_{1.99}F_{0.01}$). In this case, identifying polaronic configurations requires a specialized approach to capture the configurational disorder introduced by multiple defects, and to determine the most favorable polaron-defect coupled configuration. [68–70,84].

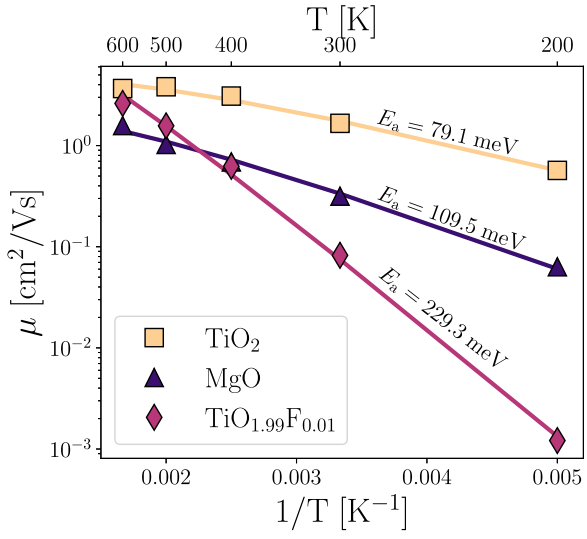

FIG. 3. Polaron mobility μ extracted from the mean squared displacement through the Einstein-relation from ns MLMD canonical ensemble (i.e., constant number of particles N, volume V and temperature T) simulations at various temperatures for $TiO_2 + e^-$, $MgO + h^+$, and $TiO_{1.99}F_{0.01}$.

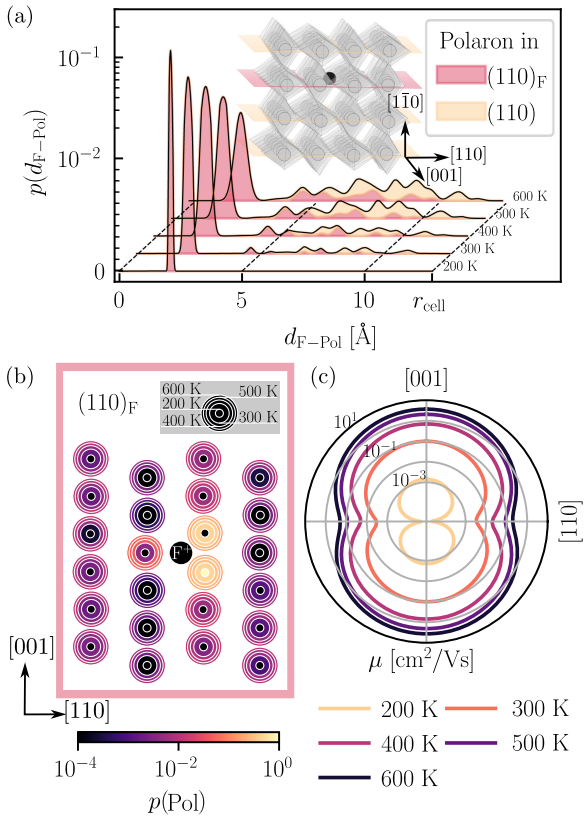

FIG. 4. Polaron defect interaction and charge mobility anisotropy in $TiO_{1.99}F_{0.01}$ from 10 ns long MLMD at different temperatures. (a) F-polaron distance distribution; light (yellow) and dark (pink) planes show contributions from different planes highlighting preferential polaron localization in the F-aligned $(110)_F$ plane and increasing interlayer mobility with rising temperature. (b) Layer-projected site distributions of polaron in $(110)_F$. Innermost circles show distribution at 200 K and consecutively larger circles show distribution at 300, 400, 500, and 600 K. (c) Polar plot of the polaron mobility μ in the $(110)_F$ plane at different temperatures along [001] and [110] directions.

Polaron trajectory data collected from 10 ns MLMD simulations indicate a strong attractive interaction between the mobile electron polaron and the immobile fluorine impurity, as suggested by the short distance peak in the polaron-fluorine radial distribution function shown in Fig. 4(a). The attractive interaction between the electron polaron and the positively charged F defect is evident in the tendency of the polaron to remain near the F defect, restricting its movement within the $(1\bar{1}0)$ basal plane containing the F atom. The polaron probability distribution displayed in Fig. 4(b) reveals that the polaron predominantly occupies the Ti sites along the [001] direction adjacent to the F defect. As the temperature increases, the probability of the polaron visiting other sites, including adjacent planes, also increases. However, the short-distance polaron-F complex remains the most favorable configuration. This result is in good agreement with previous experiments based on electron paramagnetic resonance and electron-nuclear double resonance, which identified the polaronic ground state at low temperatures as the Ti^{3+} ion adjacent to a F^- ion [78].

Furthermore, we show the direction resolved analysis of polaron mobility on $(1\bar{1}0)$ plane. The resulting polar plot displayed in Fig. 4(c) indicates a strong anisotropy with a preference of the polaron to diffuse in the [001] in agreement with the direction-dependent activation energies in TiO_2 shown in Fig. 2(d). This behavior is in very good agreement with bulk conductivity measurement [85].

Finally, we tested the scalability of our model by performing additional calculations on twice larger F-doped TiO_2 supercells, without retraining, and obtained very good performance, as discussed in SM [63].

Conclusions—To conclude, we developed a machine learning approach to study small polarons dynamics at the nanosecond timescale. Training our model on polaronic FPMD data reproduces the adiabatic and diabatic polaron transport in two structurally different polaronic materials, MgO and TiO_2, capturing both electron and hole polaron dynamics, as well as polaron-defect correlation. Our model enables an efficient and comprehensive exploration of polaron hopping pathways, providing substantially increased statistical sampling compared to first-principles MD and offering a dynamic representation of the hopping process. Mobilities, activation barriers, and diffusion anisotropies are in good qualitative agreement with previous theoretical results and explain measured experimental data. The designed ML-aided architecture is general and applicable to other systems, including charge transport in organic semiconductors and Li-ion battery materials, and can be extended to even more complex situations, such as multipolaron systems, surfaces with adsorbates, and exciton-polaron materials. More efficient generation of training data could eliminate the need for initial FPMD runs, thereby reducing the number of required DFT calculations, allowing for the use of more accurate functionals. At high polaron concentrations, where accounting for configurational disorder becomes important, employing models to sample polaron-polaron and polaron-defect configurations [68,69,84] could streamline the creation of reference databases and improve the accuracy of simulations when scaling to larger systems. Furthermore, the generality of the model could be enhanced by incorporating diabatic effects in a more rigorous form by going beyond the BO approximation.

Acknowledgments—We thank Dominik Freinberger for useful discussions and initial contributions. This research was funded by the Austrian Science Fund (FWF) 10.55776/F8100 project TACO and FWF Project No. I 4506 (FWO-FWF joint project). C. F. and L. L. acknowledge support by the National Recovery and Resilience Plan (NRRP), Mission 4 Component 2 Investment 1.3-Project NEST (Network 4 Energy Sustainable Transition) and CN-HPC Grant No. (CUP) J33C22001170001, SPOKE 7, of Ministero dell'Università e della Ricerca (MUR), funded by the European Union—NextGenerationEU. V. B. gratefully acknowledges funding from the Vienna Doctoral School in Physics (VDSP). The computational results presented have been achieved using the Vienna Scientific Cluster (VSC). We acknowledge access to LEONARDO at CINECA, Italy, via an AURELEO (Austrian Users at LEONARDO supercomputer) project.

V. B. and L. L. contributed equally to this work.

Data availability—The data that support the findings of this Letter are openly available [86].

[1] L. D. Landau, Phys. Z. Sowjet. **3**, 664 (1933).
[2] S. I. Pekar, Zh. Eksp. Teor. Fiz. **16**, 341 (1946).
[3] A. S. Alexandrov and J. T. Devreese, *Advances in Polaron Physics* (Springer, New York, 2010).
[4] A. L. Shluger and A. M. Stoneham, J. Phys. Condens. Matter **5**, 3049 (1993).
[5] C. Franchini, M. Reticcioli, M. Setvin, and U. Diebold, Nat. Rev. Mater. **6**, 560 (2021).
[6] J. B. Varley, A. Janotti, C. Franchini, and C. G. Van de Walle, Phys. Rev. B **85**, 081109(R) (2012).
[7] M. Baskurt, P. Erhart, and J. Wiktor, J. Phys. Chem. Lett. **15**, 8549 (2024).
[8] A. J. Tanner, B. Wen, Y. Zhang, L.-M. Liu, H. H. Fielding, A. Selloni, and G. Thornton, Phys. Rev. B **103**, L121402 (2021).
[9] C. Di Valentin, G. Pacchioni, and A. Selloni, J. Phys. Chem. C **113**, 20543 (2009).
[10] M. Reticcioli, I. Sokolović, M. Schmid, U. Diebold, M. Setvin, and C. Franchini, Phys. Rev. Lett. **122**, 016805 (2019).
[11] Z. Ren, Z. Shi, H. Feng, Z. Xu, and W. Hao, Adv. Sci. **11**, 2305139 (2023).

[12] S. Bandaranayake, A. Patnaik, E. Hruska, Q. Zhu, S. Das, and L. R. Baker, ACS Appl. Mater. Interfaces **16**, 41616 (2024).
[13] H. Zhang and N.-G. Park, J. Phys. **5**, 024002 (2023).
[14] H. D. Luong, T. L. Tran, V. B. T. Phung, and V. A. Dinh, J. Sci. Adv. Mater. Dev. **7**, 100410 (2022).
[15] I. Austin and N. Mott, Adv. Phys. **18**, 41 (1969).
[16] R. Marcus and N. Sutin, Biochim. Biophys. Acta **811**, 265 (1985).
[17] D. Emin and T. Holstein, Ann. Phys. (Berlin) **53**, 439 (1969).
[18] T. Holstein, Ann. Phys. (Berlin) **8**, 325 (1959).
[19] R. A. Marcus, Rev. Mod. Phys. **65**, 599 (1993).
[20] N. A. Deskins and M. Dupuis, Phys. Rev. B **75**, 195212 (2007).
[21] P. M. Kowalski, M. F. Camellone, N. N. Nair, B. Meyer, and D. Marx, Phys. Rev. Lett. **105**, 146405 (2010).
[22] A. S. Mishchenko, N. Nagaosa, G. De Filippis, A. de Candia, and V. Cataudella, Phys. Rev. Lett. **114**, 146401 (2015).
[23] S. Fratini and S. Ciuchi, Phys. Rev. Lett. **91**, 256403 (2003).
[24] S. Giannini, A. Carof, M. Ellis, H. Yang, O. G. Ziogos, S. Ghosh, and J. Blumberger, Nat. Commun. **10**, 3843 (2019).
[25] A. Troisi, Chem. Soc. Rev. **40**, 2347 (2011).
[26] B. K. Chang, J.-J. Zhou, N.-E. Lee, and M. Bernardi, npj Comput. Mater. **8**, 63 (2022).
[27] M. J. Schilcher, P. J. Robinson, D. J. Abramovitch, L. Z. Tan, A. M. Rappe, D. R. Reichman, and D. A. Egger, ACS Energy Lett. **6**, 2162 (2021).
[28] J. M. Frost, Phys. Rev. B **96**, 195202 (2017).
[29] J.-J. Zhou and M. Bernardi, Phys. Rev. Res. **1**, 033138 (2019).
[30] S. Miladić and N. Vukmirović, Phys. Rev. B **107**, 184315 (2023).
[31] V. Coropceanu, J. Cornil, D. A. da Silva Filho, Y. Olivier, R. Silbey, and J.-L. Brédas, Chem. Rev. **107**, 926 (2007).
[32] F. Ortmann, F. Bechstedt, and K. Hannewald, Phys. Status Solidi (b)**248**, 511 (2011).
[33] Y. Natanzon, A. Azulay, and Y. Amouyal, Isr. J. Chem. **60**, 768 (2020).
[34] C. Spreafico and J. VandeVondele, Phys. Chem. Chem. Phys. **16**, 26144 (2014).
[35] A. Einstein, *Investigations on the Theory of Brownian Movement* (Dover Publications, New York, 1956).
[36] R. Car and M. Parrinello, Phys. Rev. Lett. **55**, 2471 (1985).
[37] M. Setvin, C. Franchini, X. Hao, M. Schmid, A. Janotti, M. Kaltak, C. G. Van de Walle, G. Kresse, and U. Diebold, Phys. Rev. Lett. **113**, 086402 (2014).
[38] X. Hao, Z. Wang, M. Schmid, U. Diebold, and C. Franchini, Phys. Rev. B **91**, 085204 (2015).
[39] M. Reticcioli, M. Setvin, X. Hao, P. Flauger, G. Kresse, M. Schmid, U. Diebold, and C. Franchini, Phys. Rev. X **7**, 031053 (2017).
[40] M. Reticcioli, M. Setvin, M. Schmid, U. Diebold, and C. Franchini, Phys. Rev. B **98**, 045306 (2018).
[41] D. Zhang, Z.-K. Han, G. E. Murgida, M. V. Ganduglia-Pirovano, and Y. Gao, Phys. Rev. Lett. **122**, 096101 (2019).
[42] J. Wiktor, F. Ambrosio, and A. Pasquarelloj, ACS Energy Lett. **3**, 1693 (2018).
[43] S. Selcuk and A. Selloni, Nat. Mater. **15**, 1107 (2016).
[44] C. Cheng, Y. Zhu, Z. Zhou, R. Long, and W.-H. Fang, npj Comput. Mater. **8**, 148 (2022).
[45] Z.-F. Xu, C.-J. Tong, R.-t. Si, G. Teobaldi, and L.-M. Liu, J. Phys. Chem. Lett. **13**, 857 (2022).
[46] Z. Xu, C. Tong, R. Si, G. Teobaldi, and L. Liu, ChemPhysMater **2**, 331 (2023).
[47] H.-M. Wang, X.-B. Liu, S.-Q. Hu, D.-Q. Chen, Q. Chen, C. Zhang, M.-X. Guan, and S. Meng, Sci. Adv. **9**, eadg3833 (2023).
[48] A. Stuchebrukhov, J. Phys. Chem. B **120**, 1408 (2016).
[49] J. Behler and M. Parrinello, Phys. Rev. Lett. **98**, 146401 (2007).
[50] A. P. Bartók, M. C. Payne, R. Kondor, and G. Csányi, Phys. Rev. Lett. **104**, 136403 (2010).
[51] P. Friederich, F. Häse, J. Proppe, and A. Aspuru-Guzik, Nat. Mater. **20**, 750 (2021).
[52] O. T. Unke, S. Chmiela, H. E. Sauceda, M. Gastegger, I. Poltavsky, K. T. Schütt, A. Tkatchenko, and K.-R. Müller, Chem. Rev. **121**, 10142 (2021).
[53] I. Batatia, D. P. Kovacs, G. Simm, C. Ortner, and G. Csanyi, Adv. Neural Inf. Process. Syst. **35**, 11423 (2022).
[54] S. Batzner, A. Musaelian, L. Sun, M. Geiger, J. P. Mailoa, M. Kornbluth, N. Molinari, T. E. Smidt, and B. Kozinsky, Nat. Commun. **13**, 2453 (2022).
[55] M. Eckhoff, K. N. Lausch, P. E. Blöchl, and J. Behler, J. Chem. Phys. **153**, 164107 (2020).
[56] B. Deng, P. Zhong, K. Jun, J. Riebesell, K. Han, C. J. Bartel, and G. Ceder, Nat. Mach. Intell. **5**, 1031 (2023).
[57] T. W. Ko, J. A. Finkler, S. Goedecker, and J. Behler, Nat. Commun. **12**, 398 (2021).
[58] T. W. Ko, J. A. Finkler, S. Goedecker, and J. Behler, J. Chem. Theory Comput. **19**, 3567 (2023).
[59] J. Bradbury, R. Frostig, P. Hawkins, M. J. Johnson, C. Leary, D. Maclaurin, G. Necula, A. Paszke, J. VanderPlas, S. Wanderman-Milne, and Q. Zhang, JAX: composable transformations of Python + NumPy programs (2018), http://github.com/jax-ml/jax.
[60] G. Kresse and J. Furthmüller, Phys. Rev. B **54**, 11169 (1996).
[61] G. Kresse and J. Furthmüller, Comput. Mater. Sci. **6**, 15 (1996).
[62] R. Zubatyuk, J. S. Smith, B. T. Nebgen, S. Tretiak, and O. Isayev, Nat. Commun. **12**, 4870 (2021).
[63] See Supplemental Material at http://link.aps.org/supplemental/10.1103/PhysRevLett.134.216301 for detailed description of the architecture and DFT computations, which includes Refs. [64–77].
[64] H. Tang, K. Prasad, R. Sanjinès, P. E. Schmid, and F. Lévy, J. Appl. Phys. **75**, 2042 (1994).
[65] J. G. Smith, J. Naruse, H. Hiramatsu, and D. J. Siegel, Chem. Mater. **29**, 3152 (2017).
[66] A. Lempicki, Proc. Phys. Soc. London Sect. B **66**, 281 (1953).
[67] H. Kathrein and F. Freund, J. Phys. Chem. Solids **44**, 177 (1983).
[68] V. C. Birschitzky, F. Ellinger, U. Diebold, M. Reticcioli, and C. Franchini, npj Comput. Mater. **8**, 125 (2022).
[69] V. C. Birschitzky, I. Sokolović, M. Prezzi, K. Palotás, M. Setvín, U. Diebold, M. Reticcioli, and C. Franchini, npj Comput. Mater. **10**, 89 (2024).

[70] Z. Li, N. Xu, Y. Zhang, W. Liu, J. Wang, M. Ma, X. Fu, X. Hu, W. Xu, and Z.-K. Han, J. Phys. Chem. Lett. **15**, 5868 (2024).
[71] G. Kresse and D. Joubert, Phys. Rev. B **59**, 1758 (1999).
[72] P. E. Blöchl, Phys. Rev. B **50**, 17953 (1994).
[73] J. P. Perdew, K. Burke, and M. Ernzerhof, Phys. Rev. Lett. **77**, 3865 (1996).
[74] S. Falletta and A. Pasquarello, npj Comput. Mater. **8**, 263 (2022).
[75] S. Nosé, J. Chem. Phys. **81**, 511 (1984).
[76] D. P. Kingma and J. Ba, arXiv:1412.6980.
[77] S. S. Schoenholz and E. D. Cubuk, in *Advances in Neural Information Processing Systems* (Curran Associates, Inc., New York, 2020), Vol. 33.
[78] S. Yang and L. E. Halliburton, Phys. Rev. B **81**, 035204 (2010).
[79] S. Yang, A. T. Brant, N. C. Giles, and L. E. Halliburton, Phys. Rev. B **87**, 125201 (2013).
[80] K. Morita, M. J. Golomb, M. Rivera, and A. Walsh, Chem. Mater. **35**, 3652 (2023).
[81] E. Yagi, R. R. Hasiguti, and M. Aono, Phys. Rev. B **54**, 7945 (1996).
[82] E. Hendry, F. Wang, J. Shan, T. F. Heinz, and M. Bonn, Phys. Rev. B **69**, 081101(R) (2004).
[83] A. Fujishima, X. Zhang, and D. A. Tryk, Surf. Sci. Rep. **63**, 515 (2008).
[84] Y. Zhang, Z.-K. Han, B. Zhu, X. Hu, M. Troppenz, S. Rigamonti, H. Li, C. Draxl, M. V. Ganduglia-Pirovano, and Y. Gao, Nanoscale **17**, 4531 (2025).
[85] O. Byl and J. T. Yates, J. Phys. Chem. B **110**, 22966 (2006).
[86] V. Birschitzky, L. Leoni, M. Reticcioli, and C. Franchini, Quantummaterialsmodelling/leopold: Data and code for: "machine learning small polaron dynamics", (2025), 10.5281/zenodo.15302762.
[87] S. L. Dudarev, G. A. Botton, S. Y. Savrasov, C. J. Humphreys, and A. P. Sutton, Phys. Rev. B **57**, 1505 (1998).

End Matter

Appendix: Model—Most ML models, including message-passing neural networks, distinguish atoms based on their chemical species using a one-hot encoded vector of the nuclear charge Z_i but do not account for oxidation states. Since small polarons discretely alter the oxidation state by ± 1, we can encode each atom's charge state in the input one-hot encoded vector of LEOPOLD. The charge state $\mathbf{c}$ is determined through the following relation:

$$c_i = \begin{cases} 1, & \text{if } i = \arg\ \max_j |m_j| \\ 0, & \text{otherwise} \end{cases}, \tag{A1}$$

where c_i is the charge state of atom i ($c_i = 1$ for polaronic site, 0 for nonpolaronic sites) and m_j is the magnetization of atom j. In the "polaron encoding" (as shown in Fig. 5), the value c_i is appended to the one-hot encoded vector representing the species of atom i. The resulting encoding vector in a polaronic binary compound is a three-dimensional vector [e.g., in TiO_2, $\mathrm{Ti} = (1,0,0)$, $\mathrm{O} = (0,1,0)$, $\mathrm{Ti}^{\mathrm{pol}} = (1,0,1)$]. The description can easily be generalized to systems with n polarons by assigning $c_i = 1$ to the n maximally magnetized atoms.

Polarons can hop to adjacent sites when more favorable local bonding geometries enhance the adiabatic electronic coupling. To capture these dynamics, which are not reflected in the discrete encoding of charge states, LEOPOLD learns the local charge occupation of each site through the architecture reported in Fig. 5. This approach serves two key purposes: it enables tracking and updating of the polaronic states, while also regularizing the learned representation to incorporate polaronic state information. This is done by learning the occupation matrix $\mathbf{n}$, defined as

$$n^{\sigma}_{lmm'} = \sum_i f_i \langle \psi^{\sigma}_i | P^{\sigma}_{lmm'} | \psi^{\sigma}_i \rangle, \tag{A2}$$

where ψ_i are the Kohn-Sham states, f_i their occupations, l the atom index, m the specific projector function, and σ the spin channel. We use p-state projectors for $MgO + h^+$ and d-state projectors for pristine and F-doped TiO_2, as defined in DFT + U [87]. We checked that, instead of predicting

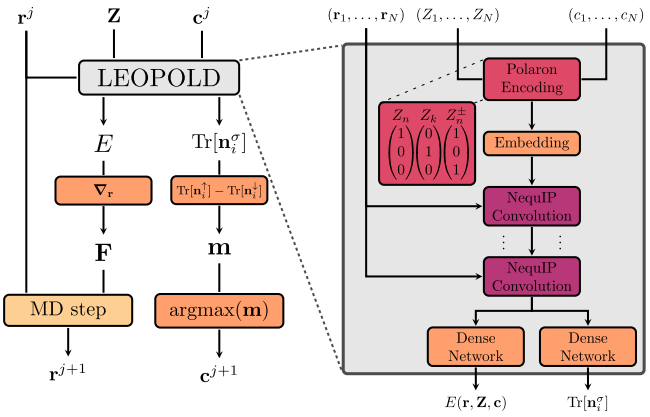

FIG. 5. Overview of workflow and model architecture. The left side shows the applied MLMD workflow, where predicted energies E and forces $\mathbf{F}$ are used to integrate the nuclei's equations of motion, while predicted occupations $\mathrm{Tr}[\mathbf{n}_i^\sigma]$ and derived magnetizations $\mathbf{m}$ determine the charge state $\mathbf{c}^{j+1}$ at the next time step. The right side shows the model architecture of LEOPOLD. Positions $\mathbf{r}^j$, nuclear charges $\mathbf{Z}$, and charge states $\mathbf{c}^j$ are fed into the neural network. The polaron encoding appends the one-hot encoded nuclear charge Z_j and charge state c_j of each atom to represent the polaronic state of the system (the enlargement shows possible vectors in a binary polaronic compound, where Z_n^{pol} encodes a polaronic atom).

the full occupation matrix, it is sufficient to learn the invariant atomic quantity $\mathrm{Tr}[\mathbf{n}_i^\sigma]$ for each atom i and spin channel σ, denoted as n_i^σ. Since small polarons carry a spin, to stabilize the prediction of the charge occupations we impose constraints ensuring that the total occupation $n_i^\uparrow + n_i^\downarrow$, the magnetization $n_i^\uparrow - n_i^\downarrow = m_i$, and the total magnetization of the system $\sum_i n_i^\uparrow - n_i^\downarrow$ are also fitted to the reference data. For details on the machine learning methodology, see SM [63].